Roya Shademani
Parviz Ghadimi

http://dx.doi.org/10.21278/brod67101

ISSN 0007-215X
eISSN 1845-5859

ESTIMATION OF WATER ENTRY FORCES, SPRAY PARAMETERS AND SECONDARY IMPACT OF FIXED WIDTH WEDGES AT EXTREME ANGLES USING FINITE ELEMENT BASED FINITE VOLUME AND VOLUME OF FLUID METHODS

UDC 629.5(05):517.9:532.5:532.585
Original scientific paper

Summary

In this paper, water entry of wedges with deadrise angles ranging from 10 to 80 degrees at two different velocities is simulated. Impact forces, spray parameters, cavity formation above the chine, and secondary impact forces due to the cavity formation are investigated with particular focus on the extreme angles. To this end, a two dimensional two-phase Finite-Element based Finite-Volume (FEM-FVM) code is developed and validated against experimental data with good compliance. Free surface modeling in this software is accomplished by applying Volume of Fluid (VOF) method. In addition to the extraction of impact forces, secondary impact forces, spray characteristics, and cavity formation, it is demonstrated that there is a combined critical length and entry velocity where the spray formation stops and the spray vanishes. It is also shown that the cavity and secondary impact do not occur under these circumstances. Moreover, it is concluded that for these particular cases, there is a maximum secondary impact force that occurs for the deadrises angles less than 20^{o}.

Key words: *Wedge water entry; FEM-FVM; VOF; Impact; Spray; Extreme angles; Secondary Impact*

1. Introduction

Water entry of hull sections in marine industries can be simplified to the water entry of wedges of different apex angles otherwise known as deadrise angles in marine applications. The importance of water entry problem is due to the fact that huge forces act on the objects during this phenomenon. These forces may end up damaging the object in question. However, if properly controlled, they can also be used in a beneficial manner. As a practical example, the lifting force acting on planning boats is indeed the water entry force exerted on the hull entering the water at high speeds with a slight angle relative to the water surface. This method

of addressing the lifting force of planning hulls is utilized in the 2D+t theory for analyzing the complex behavior of high speed crafts.

The stated applications of this problem among others have lead many researchers to focus on this apparently simple, but highly complex phenomenon. Recently, the efforts of many researchers in the field have vastly been directed towards the hydro-elastic study of the wedge water entry. For instance, Panciroli [1, 2] analyzed the water entry of flexible wedges, while Piro et al. [3] addressed the water entry and exit of flexible bodies. Other researchers who have studied this issue are Khabakhpasheva et al. [4], Yamada et al. [5], Alaoui et al. [6], Luo et al. [7][8], Mo et al. [9], and Mutsuda et al. [10].

However, there still remain unknown corners in the pure hydrodynamics of the water entry problem which require astute attention of the scientific communities. This is indeed why the researchers are still working on this issue. Yang et al. [11] numerically investigated the vertical and oblique water entry of 3D bodies using CIP-based finite difference method in 2012. Wu [12] investigated the water entry problem with varying speed. The free surface shape, jet and pressure were recently simulated by Wang et al. [13] using the Boundary Element Method. Luo et al. [14] applied an explicit finite element code to calculate the water entry loads on wedges. Velocity potential theory was used by Gao et al. [15] to simulate this problem. Ghadimi et al. [16] introduced an analytical solution for the water entry of wedges using the Schwartz-Christoffel conformal mapping. Sun et al. [17] by the use of Boundary Element Method calculated the forces acting on a planning hull through the integration of water entry force on the wedges. List of other researchers who have worked on this problem in the last five years include Qian et al. [18], Li et al. [19], Wu et al. [20], Xu et al. [21] and many others.

Hydrodynamics analyses of the wedge water entry has been conducted by many different methods including Finite Volume, Finite Element [14], Finite Difference [11], Smoothed Particle Hydrodynamics [22, 23, 24, 25], Boundary Element [13, 26], and analytical methods [16].

Although the cited works are limited to the last five years, any research on this field is surely indebted nearly a century of scientific efforts of many scientists around the world.

The focus of the present paper is on the numerical analysis of the water entry of wedges with extreme deadrise angles using Finite-Element based Finite-Volume Method (FEM-FVM) coupled with Volume of Fluid (VOF) method. Despite the fact that other researchers like Yang et al [27, 28, and 29] and Viviani et al. [25] have worked on this issue, but their studies have been limited to the range of 0 to 60 degrees deadrise angle. Also, in the present paper, as a main static parameter, the width of the wedge is considered constant in all deadrises, a constraint which causes the increase of the height of the wedge while increasing the deadrise.

In addition to the forces acting on the wedges, the spray parameters and the cavity formation on the chine of the wedges is of interest in this study. Cavity formation has been previously studied by other researchers like Wang et al. [30], but their studies has been limited to high speed water entry, while this phenomenon also occurs at low speeds.

In the following section, the governing equations and discretization are presented.

2. Numerical Method

Navier Stokes equations for transient, incompressible, and laminar flow with negligible dissipation effects are calculated for two-phase flow using FEM-FVM method coupled with the VOF method. Two-dimensional incompressible form of the conservation of mass is

$$\int_S \rho \vec{V}.\overrightarrow{dS} = 0 \tag{1}$$

and the conservation of momentum is:

$$\underbrace{\frac{\partial}{\partial t}\int_\Omega \rho\phi d\Omega}_{Transient} + \underbrace{\int_S \rho u\phi ds_x + \int_S \rho v\phi ds_y}_{Convection} = \underbrace{-\int_S (\Gamma \frac{\partial \phi}{\partial x} ds_x + \Gamma \frac{\partial \phi}{\partial y} ds_y)}_{Diffusion} + \underbrace{\int_\Omega \mathbf{S} d\Omega}_{Source} \tag{2}$$

where S is the closed surface bounding a control volume (Ω) and $\vec{V}$ is the velocity vector (velocity components are u and v in x and y direction, respectively) and ϕ, Γ and $\mathbf{S}$ are expressed as follows:

$$\begin{aligned} &\phi = u \quad \Gamma = \mu \quad \mathbf{S} = -\frac{\partial P}{\partial x} + \rho g_x \quad \text{in } x\text{-Momentum equation} \\ &\phi = v \quad \Gamma = \mu \quad \mathbf{S} = -\frac{\partial P}{\partial y} + \rho g_y \quad \text{in } y\text{-Momentum equation} \end{aligned} \tag{3}$$

Here, μ is the molecular kinematic viscosity. g_x and g_y are the gravitational accelerations in x and y direction, respectively, but g_x is equal to zero.

In the present work, the momentum equations are implemented in control volumes which result in four terms presented in equation (2).

Matrix coefficients related to this equation are as follows:

$$\begin{aligned} &[cd]_{3\times3} : \text{Diffusion} \\ &[ct]_{3\times3} : \text{Transition} \\ &[cc][cp]_{3\times3} : \text{Convection} \\ &[dp]_{3\times3} : \text{Source} \\ &[dd]_{3\times1} : \text{Constant} \end{aligned} \tag{4}$$

Equations (2) and (4) can be rewritten in matrix form as

$$[cd]\{\varphi\} + [ct]\{\varphi\} + [cc]\{\varphi\} + [cp]\{p\} + [dp]\{p\} + \{dd\} = 0 \tag{5}$$

Discretization of Eq. (2) is described in the following sections.

2.1. Transient term

Transient term is a volumetric parameter that is integrated over the cell volume. The integral version is transformed into differential form in time domain as:

$$\frac{\partial}{\partial t}\int_\Omega \rho\phi d\Omega = \left(\frac{\partial \rho\Phi}{\partial t}\right)_i \tilde{\Omega}_i = \frac{\rho\Phi_i - \rho\Phi_i^O}{\Delta t}\tilde{\Omega}_i \tag{6}$$

In equation (6), Φ_i indicates the nodal value of any arbitrary ϕ parameter like *u* and *v* in momentum equation, while $\tilde{\Omega}_i$ is the value of sub-volumes of each element, as shown in Fig.3. Therefore, equation (6) can be written in matrix form as

$$[ct]=\frac{\rho}{\Delta t}\begin{bmatrix}\tilde{\Omega}_1 & 0 & 0\\ 0 & \tilde{\Omega}_2 & 0\\ 0 & 0 & \tilde{\Omega}_3\end{bmatrix},\ [dd]=\frac{\rho}{\Delta t}\begin{bmatrix}\Phi_1^O\tilde{\Omega}_1\\ \Phi_2^O\tilde{\Omega}_2\\ \Phi_3^O\tilde{\Omega}_3\end{bmatrix} \tag{7}$$

Matrices $[ct]$ and $[dd]$ are updated and substituted in the assembly matrix.

2.2. Source term

In equation (2), the source term is the summation of pressure gradient and gravity effects and can be presented as for *x*-momentum and *y*-momentum as in

$$\int_\Omega \mathbf{S}d\Omega=\int_\Omega(-\frac{\partial p}{\partial x}+\rho g_x)d\Omega=-\int_S pdS_x+\int_\Omega \rho g_x d\Omega=-\sum_{k=1}^{3}N_k P_k dS_x+\rho g_x\sum_{k=1}^{3}\tilde{\Omega}_k \tag{8-a}$$

$$\int_\Omega \mathbf{S}d\Omega=\int_\Omega(-\frac{\partial p}{\partial y}+\rho g_y)d\Omega=-\int_S pdS_y+\int_\Omega \rho g_y d\Omega=-\sum_{k=1}^{3}N_k P_k dS_y+\rho g_y\sum_{k=1}^{3}\tilde{\Omega}_k \tag{8-b}$$

where the parameter g_x is zero. Bilinear interpolation method is applied for discretization of the pressure term and shape function N_k indicates the contribution of nodal values (P_1, P_2, P_3) at the integration points.

The source term is a volumetric parameter. Matrices $[dp]$ and $[dd]$ are updated at this stage.

2.3. Convection term

Discretization of the convection term on the control line *j,k* accomplished as in

$$\int_{S_{j,k}}\rho(\vec{V}.\vec{ds})\phi=(\rho\vec{V}.\vec{ds})_{j,k}\phi_{j,k} \tag{9}$$

For discretizing ϕ, using upwind difference scheme (UDS) in two directions of *x* and *y* causes false diffusion. In such a case, the application of UDS is assumed to occur in the direction of j_{up-x} and j_{up-y} at the integration point *j* shown in Fig.1. However, in order to eliminate the false diffusion problem, the upwind scheme (US) for ϕ should be applied in the flow direction at integration point *j* which is illustrated in Fig.1. Same would apply to integration point *k* at which the upwind scheme would also be applied in the designated "flow direction".

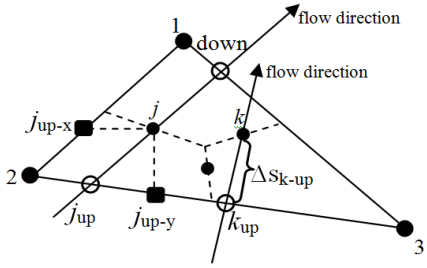

Fig.1. Flow direction in integration points

Moreover, the method proposed by Karimian and Schneider [32] is utilized which is shown in equation (10).

$$(\rho\vec{V}.\vec{ds})_{j,k}\phi_{j,k} = (\rho\vec{\hat{V}}.\vec{ds})_{j,k}\phi_{j,k} \tag{10}$$

Here, $\vec{\hat{V}}$ is the velocity vector defined by Karimian and Schnider's [32] scheme to prevent the checkerboard problem. The components of the vector are calculated using equations (11) and (12).

$$\hat{u}_j = U_{L-S} - \frac{\Delta S_U}{\rho\overline{V}}\left\{-\rho\left(u\frac{\partial v}{\partial y} - v\frac{\partial u}{\partial y}\right) + \rho\frac{\partial u}{\partial t} + \frac{\partial P}{\partial x} - \mu\overline{\nabla^2 u}\right\} \tag{11}$$

$$\hat{v}_j = V_{L-S} - \frac{\Delta S_U}{\rho\overline{V}}\left\{-\rho\left(v\frac{\partial u}{\partial x} - u\frac{\partial v}{\partial x}\right) + \rho\frac{\partial v}{\partial t} + \frac{\partial P}{\partial y} - \mu\overline{\nabla^2 v}\right\} \tag{12}$$

P is the pressure, ρ is the fluid density, ΔS_U is the distance of the integration point from the upwind point as illustrated in Fig. 1. U_{L-S} and V_{L-S} are calculated using a bilinear interpolation on the velocity. Also, the bar sign on any variable indicates the value from the previous time step. Accordingly, $\overline{V}$ is the velocity from the previous time step. The final form of the continuity equation is presented as

$$(\rho\hat{u}ds_x)_j + (\rho\hat{u}ds_x)_k + (\rho\hat{v}ds_y)_j + (\rho\hat{v}ds_y)_k = 0 \tag{13}$$

Also, in equation (10), ϕ_j is calculated using the relation

$$\phi_j = \phi_{upj} + \frac{\partial\phi}{\partial s}\Delta s \tag{14}$$

where ϕ_{upj} is the upwind velocity at integration point j, as shown in Fig. 1, and $\frac{\partial\phi}{\partial s}\Delta s$ is a linear estimation of the variation of ϕ from the upwind point to the integration point.

2.4. Diffusion term

The diffusion term is modeled as

$$-\int_{S_{j,k}} \Gamma(\overrightarrow{\nabla\phi}.\overrightarrow{dS}) = -\Gamma\overrightarrow{\nabla\phi}.\overrightarrow{ds}\Big|_{j,k} = -\left(\Gamma\frac{\partial\phi}{\partial x}ds_x + \Gamma\frac{\partial\phi}{\partial y}ds_y\right)\Big|_{j,k} \tag{15}$$

Calculations of $\frac{\partial\phi}{\partial x}$ and $\frac{\partial\phi}{\partial y}$ are performed using shape functions. These terms are determined by

$$\frac{\partial\phi}{\partial x} = \sum_{i=1}^{3}\frac{\partial N_i}{\partial x}\Phi_i \tag{16-a}$$

$$\frac{\partial\phi}{\partial y} = \sum_{i=1}^{3}\frac{\partial N_i}{\partial y}\Phi_i \tag{16-b}$$

$[cd]$ is a 3×3 matrix and each row belongs to a sub-volume, as shown in Fig. 3.

$$[cd_{j,i}] = \frac{\partial N}{\partial x}\Big|_{j,i}\times dS_x\big|_{j,j} + \frac{\partial N}{\partial x}\Big|_{k,i}\times dS_x\big|_{j,k} + \frac{\partial N}{\partial y}\Big|_{j,i}\times dS_y\big|_{j,j} + \frac{\partial N}{\partial y}\Big|_{k,i}\times dS_y\big|_{j,k} \tag{17}$$

In equation (17), *j* is the sub-volume indicator and *k* is the integration points of each sub-volume and *i* any of the three nodes that embody each element.

2.5. VOF modeling

Volume of Fluid (VOF) method is based on the conservation of volume fraction (α) with respect to time and space which is formulated as

$$\frac{\partial\alpha}{\partial t} + \frac{\partial(u\alpha)}{\partial x} + \frac{\partial(v\alpha)}{\partial y} = 0 \tag{18}$$

In the VOF method, volume fraction (α) is a scalar parameter which represents the fraction of a cell filled with one fluid, while assuming $1-\alpha$ represents the volume fraction of the second fluid. When $\alpha = 1$, the cell is filled by the first fluid and the density/viscosity of the first fluid is used. On the other hand, when $\alpha = 0$, the cell is filled by the second fluid and the properties of the second fluid is implemented. When, $0 < \alpha < 1$ the cell contains a portion of both fluids and equivalent properties should be used. To consider a general formulation of these three cases using the volume fraction approach, the equivalent density and viscosity of the cells are expressed as follows:

$$\begin{aligned}\rho_{eq} &= \alpha\rho_1 + (1-\alpha)\rho_2 \\ \mu_{eq} &= \alpha\mu_1 + (1-\alpha)\mu_2\end{aligned} \tag{19}$$

where α is the volume fraction, while ρ_1 or ρ_2 and μ_1 or μ_2 are the density and viscosity of the fluids, respectively. Physical properties are estimated by a linear mixture assumption. In finite volume method, α is calculated on each cell center and is used in governing differential equation of conservation of volume fraction function. In finite element based finite volume, nodal points of elements are utilized for applying this conservation equation. Based on these properties, the VOF method in

$$\frac{\partial}{\partial t}(\rho) + \nabla.(\rho V) = 0 \tag{20}$$

is transformed to

$$\frac{\partial \alpha}{\partial t} + V.\nabla\alpha + \alpha\nabla.V = -\frac{\rho_g \nabla.V}{(\rho_L - \rho_g)} \tag{21}$$

where $V(u,v)$ is the velocity vector. For incompressible two phase flow without any phase change, $\nabla.V$ is zero, ρ_g is the density of gas (air) and ρ_L is the density of liquid (water) and equation (21) reduces to equation (18).

If the index P denotes the center of control volume and δt represents the time interval, the finite-volume discretization of equation (18) leads to

$$\alpha_P^{t+\delta t} = \alpha_P^t + \frac{\delta t}{V_P}\sum_{f=1}^{n}\alpha_f^* Q_f \ , \tag{22}$$

where V_P is the cell volume, f is the centroid of the cell face, Q_f is the volumetric flux through the face and α_f^* is the approximation of the time-averaged volume fraction face value. Cell-centered values of α are used to interpolate the face values α_f^*. In finite element based finite volume method, integration point is used as a cell center and donor-acceptor flux approximation is utilized for simulation of α. Concept of donor-acceptor method has been described by Ubbink and Issa (1999). In the present study, this method (formulated in equation (22)) has been altered and used for unstructured mesh and finite element method. The applied method uses CICSAM scheme (Ubbink and Issa (1999)) in equation (22) based on the normalized variable diagram (NVD) which is found by the normalized values of volume fraction calculated based on the general relation

$$\tilde{\alpha} = \frac{\alpha - \alpha_U}{\alpha_A - \alpha_U} \ . \tag{23}$$

This equation can be used to normalize the volume fraction at any point like the integral point or a point which is located between two main points on the element boundary. According to equation (23), normalized volume fraction ($\tilde{\alpha}$) is presented as a function of upwind (α_U) and acceptor (α_A) nodal values. Equation (22) is solved by an iterative method based on the normalized parameters and volume fraction at nodal points is calculated using equation (23) (i.e. $\alpha = \alpha_U + \tilde{\alpha}(\alpha_A - \alpha_U)$). To calculate the normalized values at donor ($\tilde{\alpha}_D$) and acceptor ($\tilde{\alpha}_f$) points, equation (23) is utilized as follows:

$$\tilde{\alpha}_D = \frac{\alpha_D - \alpha_U}{\alpha_A - \alpha_U} = 1 + \frac{\alpha_D - \alpha_A}{2(\nabla\alpha)_D.\vec{d}}, \tag{24}$$

$$\tilde{\alpha}_f = \frac{\alpha_f - \alpha_U}{\alpha_A - \alpha_U} = 1 + \frac{\alpha_f - \alpha_A}{2(\nabla\alpha)_D.\vec{d}}, \tag{25}$$

where subscripts U, D and A indicate the upwind, donor and acceptor cells, respectively. Also, $\vec{d}$ is the vector between the cell centers of the donor and acceptor cells as presented in Fig.2 and $\alpha_U = \alpha_A - 2(\vec{\nabla}\alpha)_D.\vec{d}$.

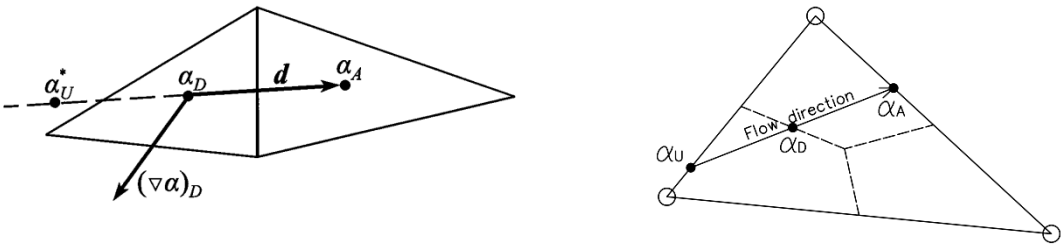

(a) (b)

Fig. 2. a) Prediction of the upwind value for an arbitrary cell arrangement (presented by Ubbink and Issa, (1999)), and b) New modification of donor-acceptor scheme.

Equation (22) is rewritten in normalized value fashion as

$$\tilde{\alpha}_P^{t+\delta t} = \tilde{\alpha}_P^t + \frac{\delta t}{V_P}\sum_{f=1}^{n}\tilde{\alpha}_f^* Q_f \tag{26}$$

where $\tilde{\alpha}_P^{t+\delta t}$ is the normalized volume fraction at a cell (sub-elements), $\tilde{\alpha}_P^t$ is the value of $\tilde{\alpha}_P$ from the previous time step and $\tilde{\alpha}_f^*$ is the approximation of time-averaged normalized volume fraction face value. Normalized values are calculated based on equations (24) and (25).

In the current study, donor-acceptor scheme is used for each sub-element. Integral points are assumed as donor cells or points (see Fig. 2b), and α is predicted based on the shape functions. Shape functions are utilized for calculating α_U based on these values at the nodal points. Three nodal values are saved for each element. Accordingly, α_U can be predicted in two ways: 1) through using shape functions in local coordinates and 2) by linear interpolation of two neighboring nodes. The second method is adopted for the current study. New values of U are updated in every time step at the integral points and flow direction is set. Subsequently, α_U and α_A are calculated and the donor-acceptor scheme is reapplied.

When using VOF method, equation (19) is implemented in place of fluid properties in the Navier-Stokes equations. This way, although the Navier-Stokes equations are solved simultaneously for both fluids as one, the free surface can be extracted using the volume fraction. Based on the initial conditions, values of α are applied on the nodal points. Subsequently, these parameters are interpolated by shape functions and estimated on the integral points. In each time step, flow pattern is generated and velocity vectors are

determined at the integral points. Consequently, donor and acceptor nodes are set and equation (22) is solved in each sub-element using normalized values. Then, new values of α are calculated based on the normalized values of α from the previous time step obtained from equation (23).

At this stage, new volume fractions of the cells located on the boundary of the two-phase flow are updated and the free surface is determined for this time step. The new values of α are calculated at integral points and are extended to the element points by shape functions. Each element has a volume fraction value that can be calculated based on three nodal points. In the visualizations, the free surface represents $\alpha = 0.5$.

The applied numerical method is briefly explained in the next section.

2.6. Finite-Element concepts

As pointed out earlier, triangular grids are used in the current study, as shown in Fig. 2. General form of a typical mesh is displayed in Fig. 3. For reducing the computing time, the origin has been moved to each integration point (*ip*) and the coordinate system (x-y) has been rotated (to s-t coordinate system) in order to place x coordinate in the direction of the velocity vector at that integration point. As a result, less computational power is required for calculations related to shape functions or geometrical characteristics of elements.

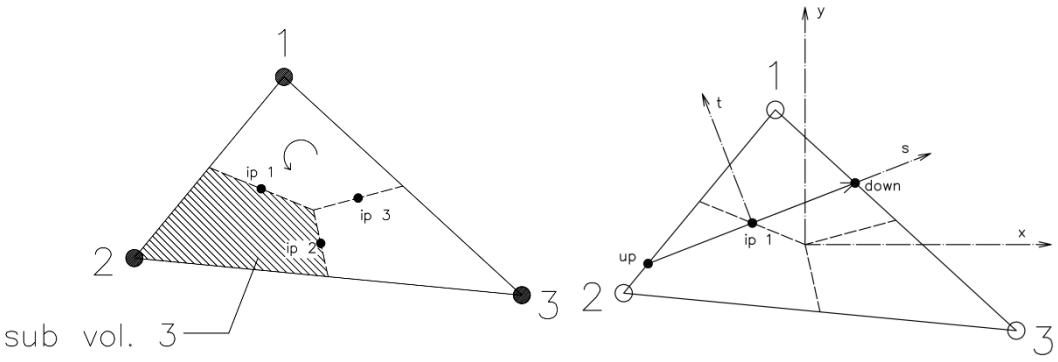

Fig. 3. A typical triangular element and calculation of up and down points of the velocity vector through the integration points.

Shape functions are defined on each node of the elements as $\phi = \sum_{i=1}^{Node} N_i \phi_i$, where N_i is the shape function at node *i*, while ϕ_i is the value of ϕ at that node. The method utilized in this paper is based on the fully coupled Rhie and Chow [31] algorithm applied on a collocated triangular grid system for a 2D fluid flow. The shape functions for the triangular elements are as follows:

$$N_1 = (\frac{y_2 - y_1}{DET})x + (\frac{x_3 - x_2}{DET})y + (\frac{x_2 y_3 - x_3 y_2}{DET})$$

$$N_2 = (\frac{y_3 - y_1}{DET})x + (\frac{x_1 - x_3}{DET})y + (\frac{x_3 y_1 - x_1 y_3}{DET}) \quad (27)$$

$$N_3 = (\frac{y_1 - y_2}{DET})x + (\frac{x_2 - x_1}{DET})y + (\frac{x_1 y_2 - x_2 y_1}{DET})$$

$$DET = (x_1 y_2 + x_2 y_3 + x_3 y_1 - y_1 x_2 - y_2 x_3 - y_3 x_1)$$

where DET is the determinant of the coordinates matrix. The involved terms in these equations are discretized on control lines between each two nodes.

The overall algorithm of the code is illustrated in Fig. 4.

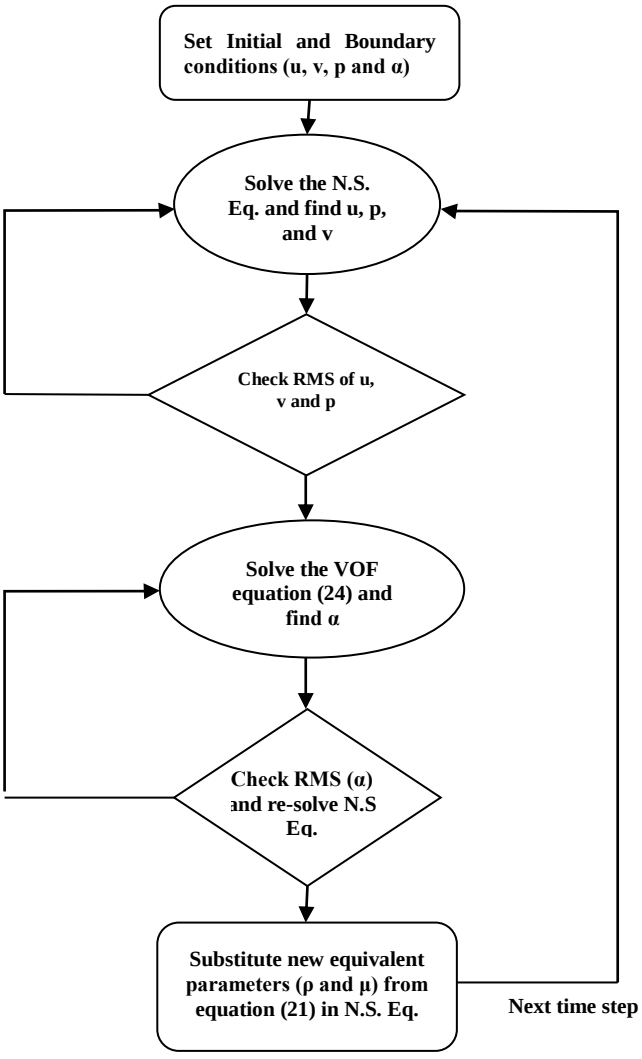

Fig. 4. Flow chart of the numerical algorithm.

As observed in Fig. 4, Navier Stokes equations are solved, first. Subsequently, the VOF equations are solved using the velocities resulting from the Navier Stokes equations. Afterward, using the obtained volume fraction, the new density and viscosity in each element are calculated and fed into the Navier Stokes equations for the next time step.

A computer code is developed based on this algorithm for solving the two phase flow problem of the wedge water entry. In the next section, the developed code is validated using previously published water entry data.

3. Validation

To validate the developed code, the experimental results provided by Tveitnes et al. [33] are utilized. The validation cases consist of two wedges with 10 and 15 degrees deadrise angles and 0.6 m width, at a vertical entry speed of 0.94 m/s. The definitions used in the validation tests and the boundary conditions are presented in Fig. 5.

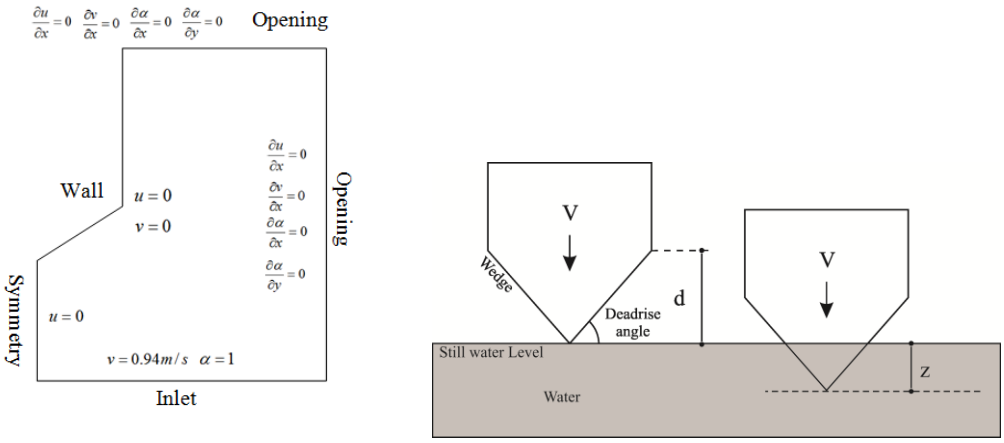

Fig. 5. Definition of boundary conditions and parameters in the validation test.

It should be mentioned that the courant number has been limited to 0.25 to avoid any errors concerning the ratio of mesh versus time step. The calculated forces compared against experimental results are illustrated in two different plots of Fig. 6.

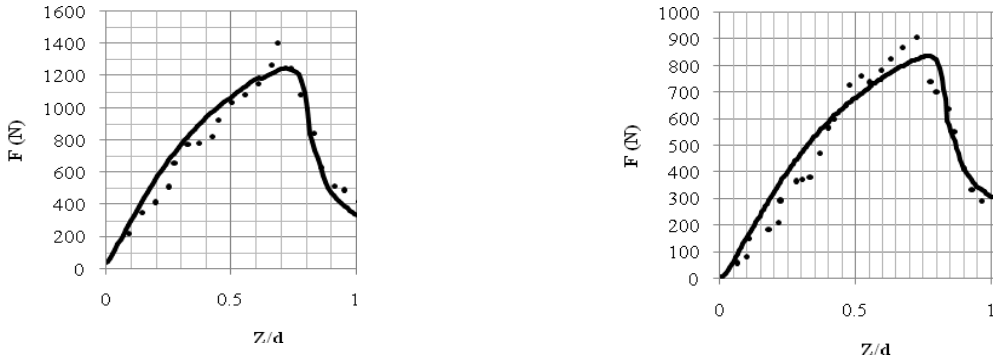

(a) (b)

Fig. 6. Water entry force (F) Vs normalized Apex depth (Z/d): Comparison of numerical results (-) versus experimental data (**.**) [33] for deadrise angles of a) 10 degrees and b) 15 degrees

As observed in Fig.6, the developed code provides reliable results for predicting the water entry forces on wedges. The mean error is about 5.36% and 7.48% for 10 and 15 degrees deadrise angle, respectively. Also, a maximum error of 10.5% and 13.4% are observed for 10 and 15 degrees deadrise angles, respectively. This seems to be a reasonable error, since water entry problem is highly nonlinear at low deadrise angles.

Tveitnes et al. [33] have also provided snap shots of the tests which are used here for validation of the free surface modeling. For better visualization purposes, the free surface has been digitized and numerical free surface has been overlaid on the experimental data.

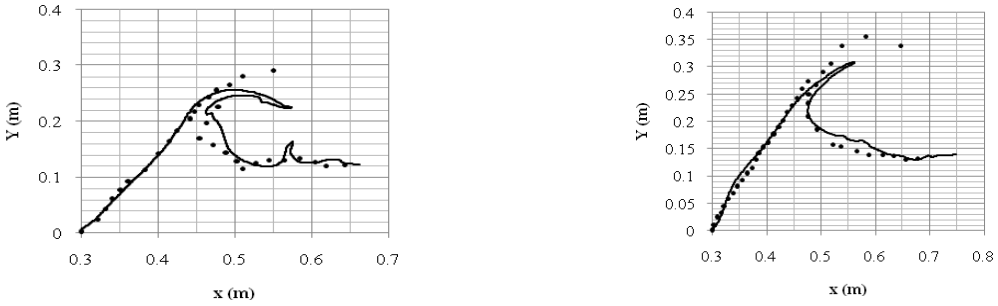

(a) (b)

Fig. 7. Free Surface: Comparison of numerical results (-) versus experimental data (**.**) [33] for a) 10 degrees (at 0.1705s after entry) and b) 15 degrees deadrise angle (at 0.2265s after entry)

As evident in Fig.7, there is a slight difference in the breaking of the spray, where the experimental spray is higher than the computed spray. This may be attributed to the fact that water drops at that point detach from the surface and cause the free surface to be nebular, a phenomenon which does not exactly occur in numerical solutions. However, there is good similarity between the simulation and the experimental data in other areas of the free surface.

In the next section, water entry of several wedges at different speeds is analyzed using the developed code.

4. Results and Discussion

Results of different analyses are presented in this section. As discussed in the introduction, the main objectives of this study is to investigate the water entry forces acting on wedges at extreme angles and the spray characteristics where the returning point occurs. The returning point, as defined in the present work, is the moment when the free surface separates from the chine and begins to return towards the wedge. This definition is better understood using the schematics of Fig.8.

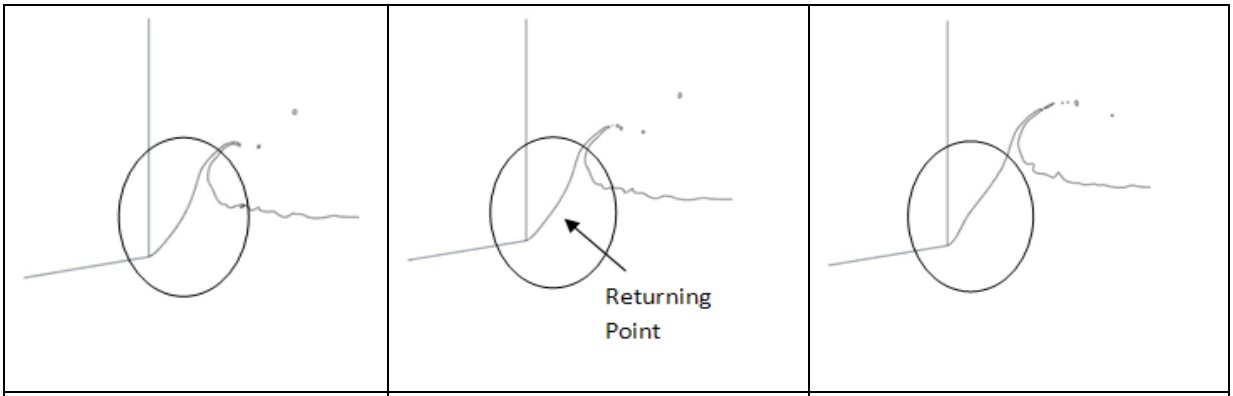

a) Before Returning Point	b) Returning Point	c) After Returning Point

Fig. 8. Definition of Returning Point

At the Returning Point, the spray parameters are defined as in Fig.7.

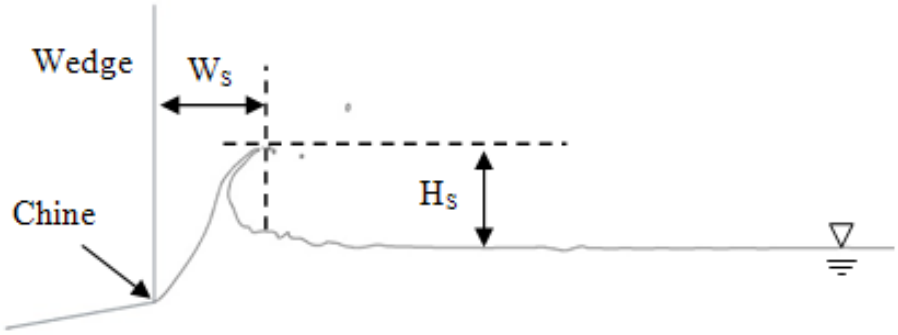

Fig. 9. Schematics of spray parameters

As demonstrated in Fig.9, W_s is the distance of the leading point of the spray.

Another phenomena which is of interest in the present work, is the air cavity formation due to the secondary impact (as shown in Fig.10). As discussed in the introduction, due to the water entry of the wedge, a low pressure region occurs above the chine which causes the water to return to the wedge. This sudden return of water entraps some air as an air cavity which sinks with the chine.

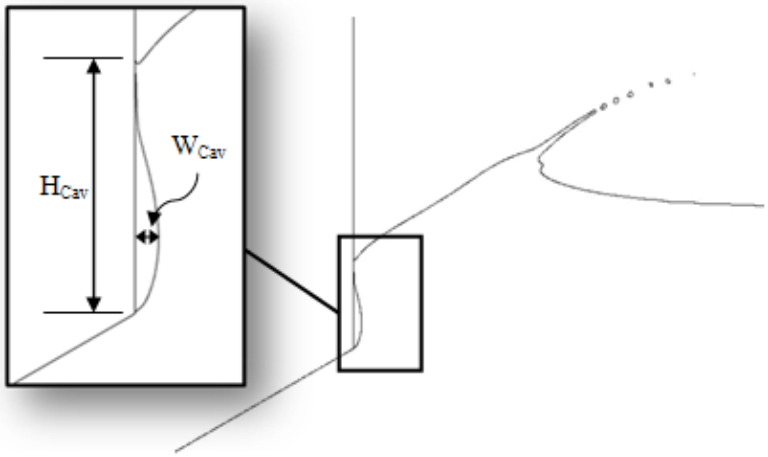

Fig. 10. Cavity formation parameters

Having defined the returning point, the spray parameters and the cavity formation parameters, the intended analyses are carried out at this stage. The water entry forces, the secondary impact forces, the air cavity parameters and the spray parameters are extracted at two different entry velocities of 1m/s and 2m/s for each deadrise angle. For all the considered cases, the width of the wedge has been set as a design constraint with a value of 1 m. This implies that the height of the wedge grows with the deadrise angle. The geometries of different wedges are illustrated in Fig.11.

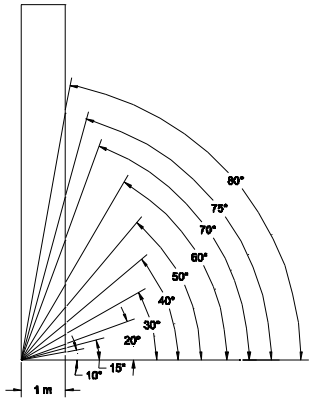

Fig. 11. Geometries of different wedges: half wedges are modeled in the simulations, due to the symmetric behavior of the wedge

4.1 Impact Forces

Based on the analyses of the considered test cases, the forces acting on the wedges are plotted in Figs.12 and 13.

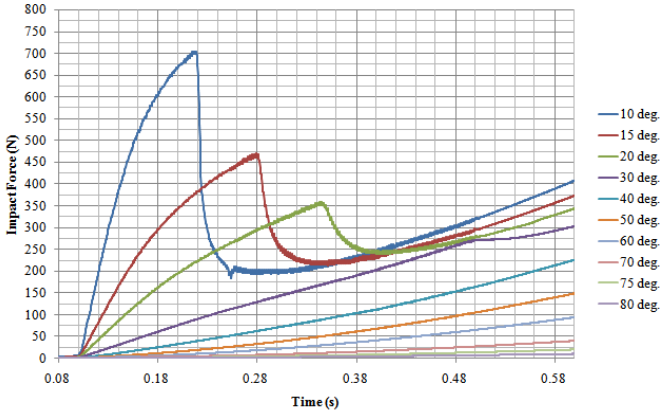

Fig. 12. Forces acting on different wedges during water entry at V = 1 m/s velocity

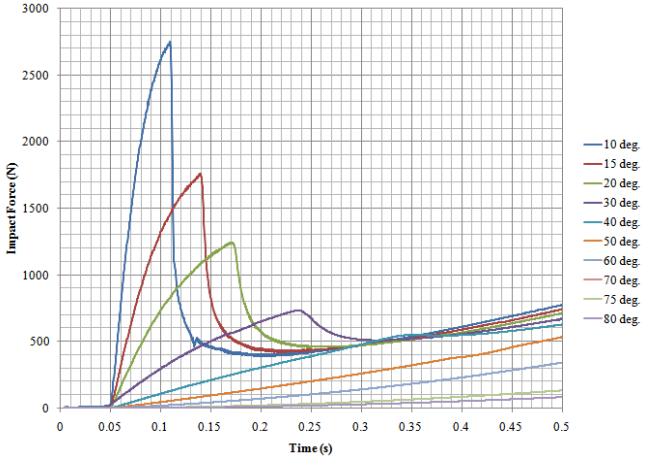

Fig. 13. Forces acting on different wedges during water entry at V = 2 m/s velocity

As evident in Figs.12 and 13, the peak of the force acting on the wedge is highly dependent on the deadrise angle of the wedge. It can be concluded that the peak force logarithmically decreases by an increase in the deadrise angle in a way that no peak occurs for the deadrise angles more that 50 degrees.

4.2 Spray Characteristics

In order to investigate the spray characteristics of the wedges, the spray parameters should be extracted at the returning point. The free surface profiles for different deadrises are presented in Fig.14.

Deadrise Angle (degree)	V = 1 m/s	V = 2 m/s
10	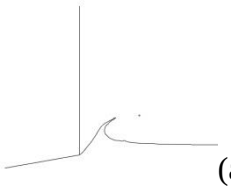 (a)	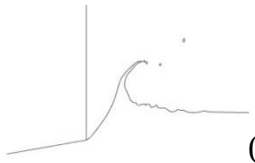 (b)
15	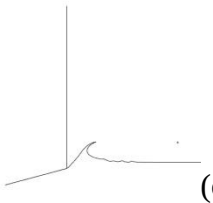 (c)	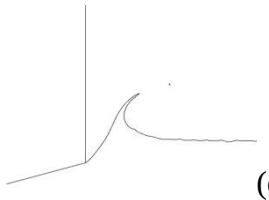 (d)
20	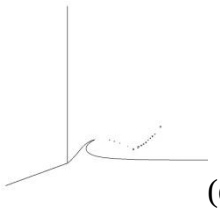 (e)	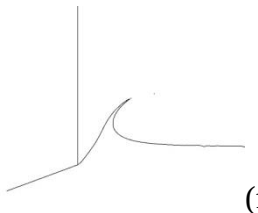 (f)
30	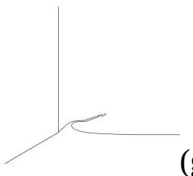 (g)	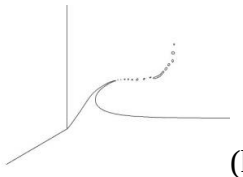 (h)
40	No Returning Point	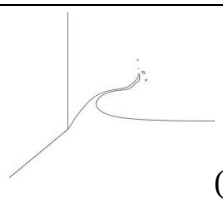 (i)
50	-	No Returning Point
60	-	-
70	-	-
75	-	-
80	-	-

Fig. 14. Profiles of the spray formed at the returning point for different deadrises and velocities

As observed in Fig.14, there is no returning point for the deadrises more than 50 deg. at 2 m/s and also for the deadrises more than 40 deg. at 1 m/s. This is due to a phenomenon which the authors believe has not yet been addressed in the literature. When the wedge enters the water, the spray root normally forms a plume which grows and after reaching the chine, the main spray forms. This procedure is depicted for the deadrise angle of 40 deg. at 2 m/s velocity in Fig.15.

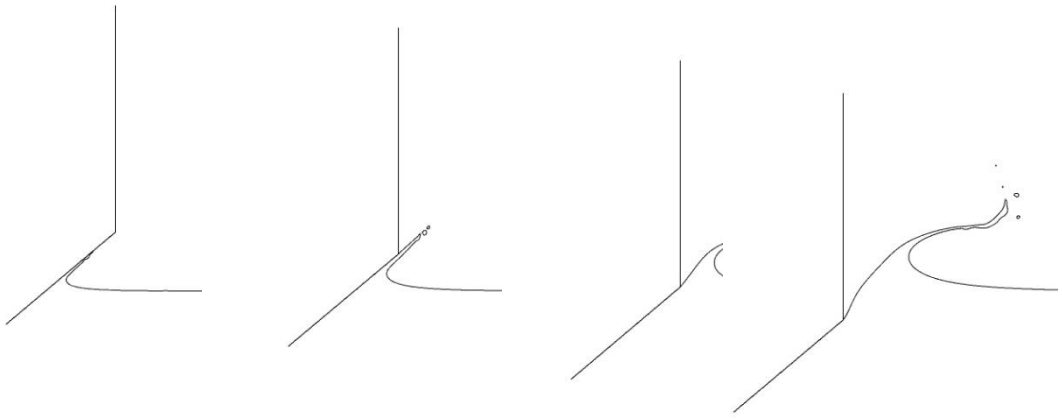

Fig. 15. Development of spray at 40^{o} deadrise angle and 2 m/s velocity: The normally expected feature

However, it has been observed that for a lower water entry velocity or a longer wedge length, the spray root may get weaker and detach from the wedge before reaching the chine. As an example, this happens for the 40 deg. wedge at 1 m/s velocity. Based on the comparison of the two velocities, one may conclude that there is a critical length for each deadrise angle at each particular velocity where the spray may vanish before reaching the chine. If this assertion is true, there should then be some kind of limitations in using the earlier analytical and empirical theories related to water entry phenomenon.

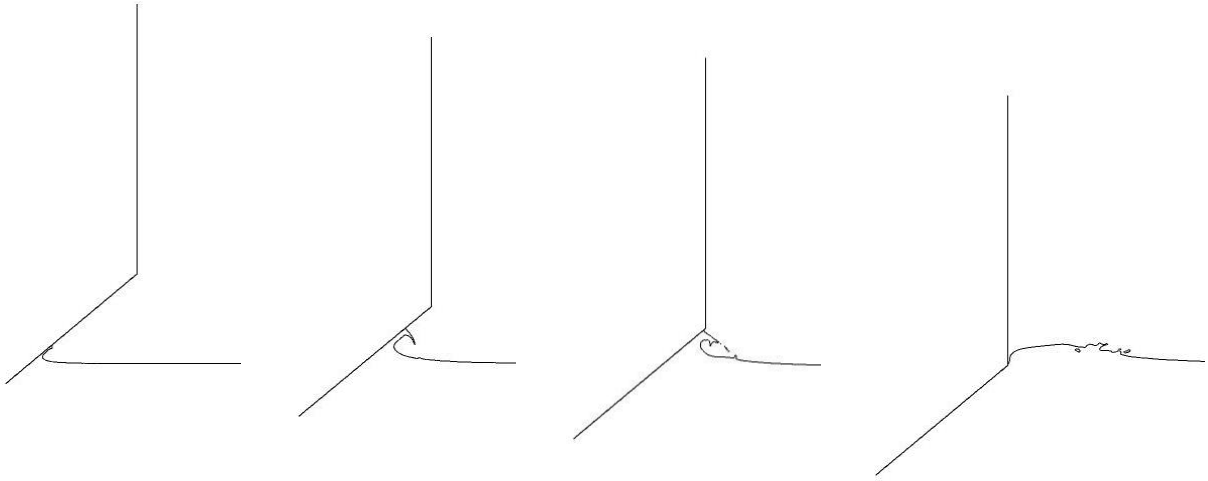

Fig. 16. Development and vanishing of spray at 40 deg. deadrise angle and 1 m/s velocity: The critical length

At higher deadrise angles, this occurs more rapidly, as observed in Fig.16. Similar behavior is displayed even more rapidly for 1 m/s velocity which is not shown here for the sake of briefness.

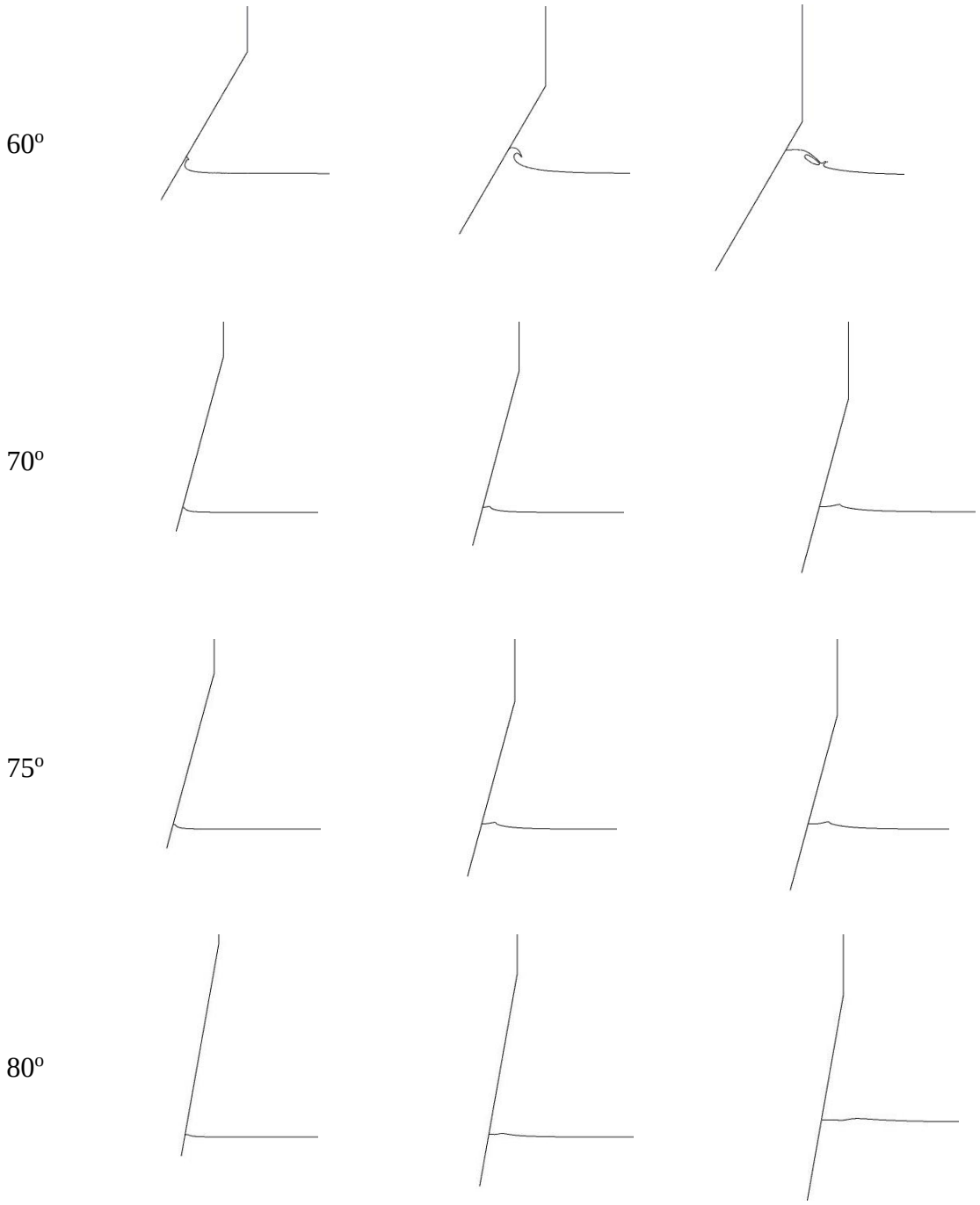

Fig. 17. Development and vanishing of spray for high deadrise angles at 2 m/s velocity: An indication of the fact that there is a critical length for each deadrise angle

As evident in Fig.17, the water elevation and spray formation is limited by the length of the wedge and/or the velocity of the water entry. Therefore, a limitation should be applied to the empirical and analytical formulas on the water entry spray, water elevation and even force and pressure calculation. However, it is not within the scope of the current study to extract the precise limitation and this should be separately investigated in future works.

The spray parameters are extracted from Fig.14 and plotted against deadrise angle and velocity in Fig.18.

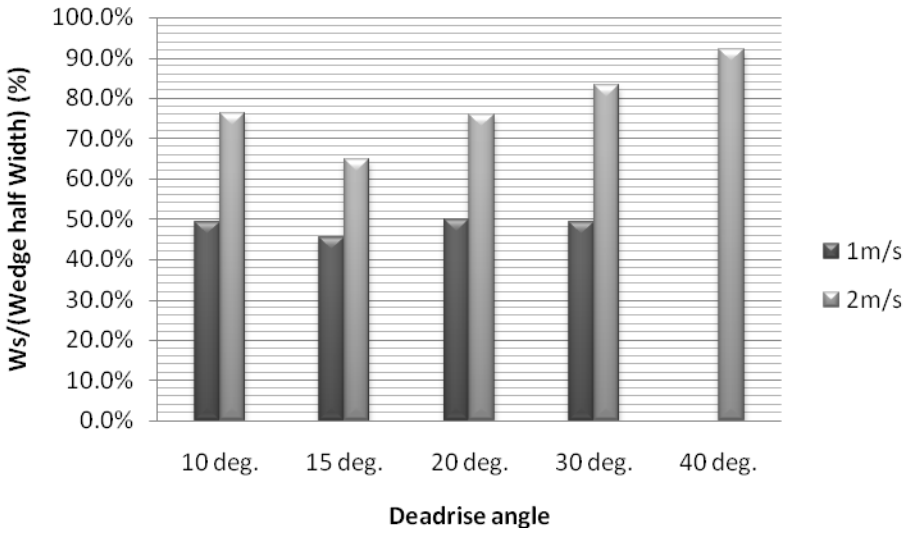

(a)

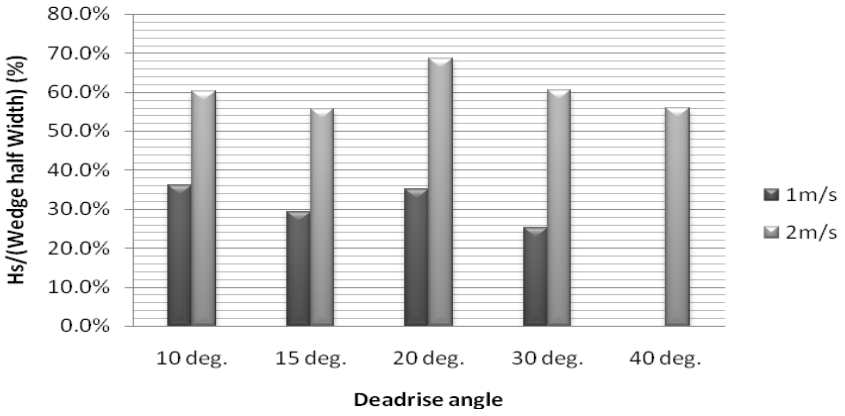

(b)

Fig. 18. The spray parameters for different deadrise angles and two velocities

As observed, the spray parameters do not linearly vary with deadrise angle. The highest spray height is produced by 10 degree deadrise for V = 1m/s and by 20 degree deadrise for V = 2m/s. Also, the lowest spray height is produced by 30 degree deadrise for V = 1m/s and by 15 degree deadrise for V = 2m/s. Same observation is made on the width of the spray where the longest spray is produced by 20 degree deadrise for V = 1m/s and by 40 degree deadrise for V = 2m/s. Also, the shortest spray width is produced by 15 degree deadrise for both velocities.

4.3 Cavity Formation and Secondary Impact Force

Another phenomenon investigated in the current study is the cavity formation above the chine which is accompanied by a secondary impact on the hull. In Fig.19, the cavity formation is illustrated at different deadrise angles.

Deadrise Angle (degree)	V = 1 m/s	V = 2 m/s
10	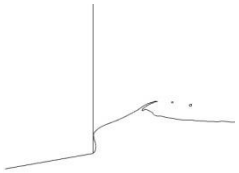 (a)	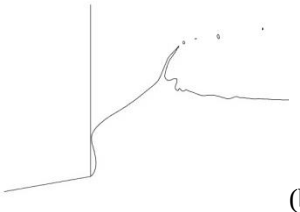 (b)
15	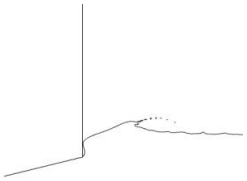 (c)	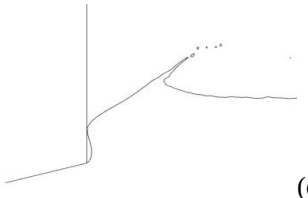 (d)
20	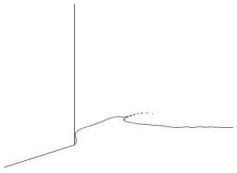 (e)	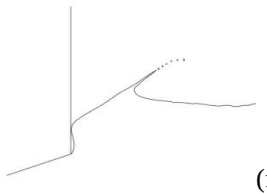 (f)
30	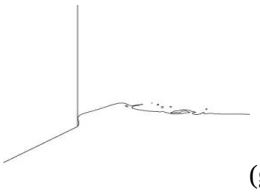 (g)	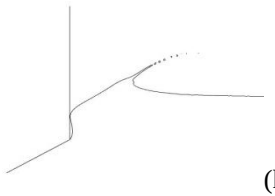 (h)
40	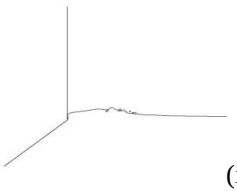 (i)	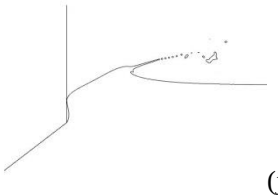 (j)
50	No cavity	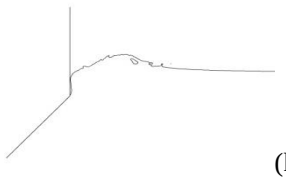 (k)
60	-	No cavity
70	-	-
75	-	-
80	-	-

Fig. 19. The cavity formation for different deadrise angles at two different velocities

As observed again, the cavity is not formed for high deadrises. The secondary impact forces are illustrated in Figs.20 and 21.

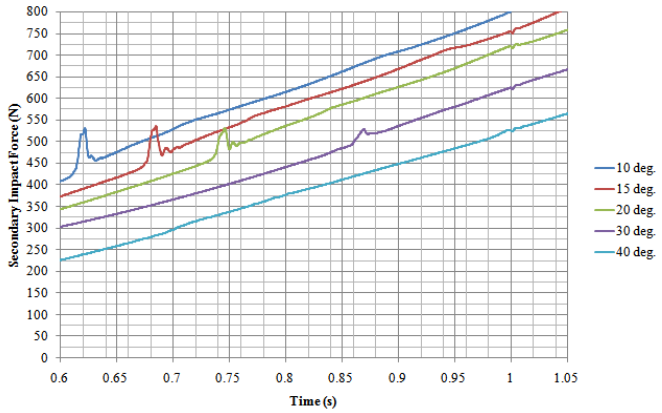

Fig. 20. Secondary impact forces at 1 m/s velocity

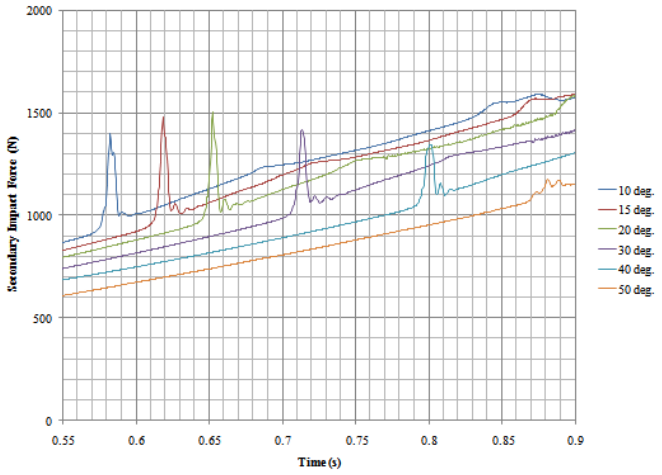

Fig. 21. Secondary impact forces at 2 m/s velocity

As expected, the cavities formed at higher velocities and lower deadrises are larger, but this does not cause higher secondary impact forces. In fact, it seems that the secondary impact force for deadrise angles under 20 degrees is not highly affected by the deadrise. Also, the secondary impact forces corresponding to 10, 15 and 20 degrees are higher than those of 30 degrees and above. This may be attributed to the secondary impact being mainly generated by tangential forces. This may also be attributed to the fact that the normal force of the water touching the wedge wall for lower deadrises is more than the larger ones and this way, the maximum frictional force is generated for the lower deadrises. In other words, there is indeed a maximum for the secondary impact forces which is affected mainly by the entry velocity.

The geometrical parameters of the cavity are extracted from the Fig.19 and plotted versus deadrise angles and velocity in Fig.22.

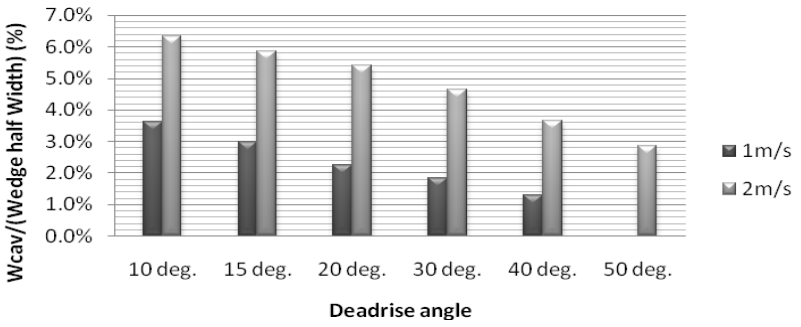

(a)

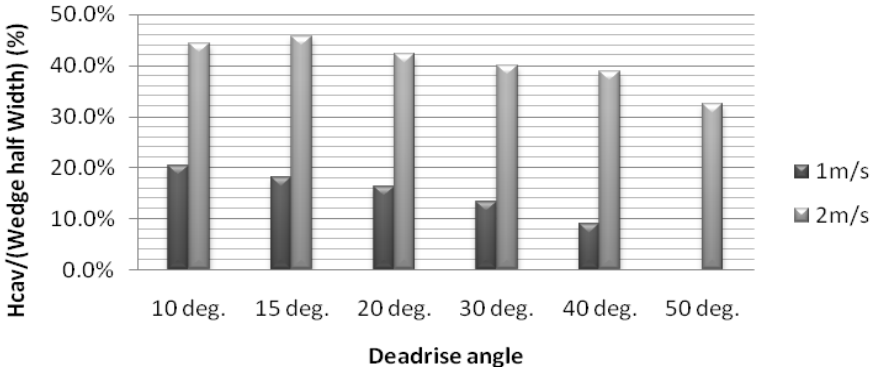

(b)

Fig. 22. The geometrical parameters of cavity for different deadrise angles at two different velocities

As expected, the width and height of the cavity diminishes with an increase in the deadrise angle, while the entry velocity highly affects the cavity sizes. Moreover, it is observed that the height of the cavity is more sensitive to the entry velocity. Contrary to the height and width of the spray, the cavity parameters seem to obey a regulated variation versus deadrise angle.

5. Conclusions

In the present paper, the Navier Stokes equations have been solved using Finite-Element based Finite-Volume method. In order to facilitate the free surface modeling of wedge water entry problem, this solver has been coupled with Volume of Fluid method (VOF). The code has been validated against experimental data with good compliance. Subsequently, the water entry problem of wedges with deadrise angles ranging from 10 to 80 degrees have been analyzed for two different entry velocities of 1 and 2 m/s. The water entry forces have been extracted and it is shown that for deadrises higher than 40^o for 1 m/s and 50^o for 2 m/s, the peak of water impact force does not occur and in fact there is no significant impact.

Also, the returning point of the free surface has been defined and used to analyze the spray formation at different deadrises and velocities. In this procedure, it is observed that the spray formation at each deadrise angle is limited by the entry velocity and the length of the wedge, and the spray may vanish before reaching the chine. This observation needs to be more accurately investigated and explored in future works.

Another phenomenon which has been addressed in the present manuscript is the cavity formation above the chine and the secondary impact forces. It has been illustrated that the cavity is larger for lower deadrise angles and higher velocities. However, it has been shown that this does not affect the amount of the force acting on wedges with deadrise angles less than 20^o, an observation which implies that there is a maximum secondary impact force which occurs in deadrises less than 20^o.

References

[1] R. Panciroli: Water entry of flexible wedges: Some issues on the FSI phenomena. Applied Ocean Research 39, p. 72-74, 2013. https://doi.org/10.1016/j.apor.2012.10.010.

[2] R. Panciroli, S. Abrate, G. Minak, A. Zucchelli: Hydroelasticity in water-entry problems: Comparison between experimental and SPH results. Composite Structures 94 (2), p. 532-539, 2012. https://doi.org/10.1016/j.compstruct.2011.08.016.

[3] D.J. Piro, K.J. Maki: Hydroelastic analysis of bodies that enter and exit water. Journal of Fluids and Structures 37, p. 134-150, 2013. https://doi.org/10.1016/j.jfluidstructs.2012.09.006.

[4] T.I. Khabakhpasheva, A. Korobkin: Elastic wedge impact onto a liquid surface: Wagner's solution and approximate models. Journal of Fluids and Structures 36, p. 32-49, 2012. https://doi.org/10.1016/j.jfluidstructs.2012.08.004.

[5] Y. Yamada, T. Takami, M. Oka: Numerical study on the slamming impact of wedge shaped obstacles considering fluid-structure interaction (FSI). Proceedings of the International Offshore and Polar Engineering Conference, 2012.

[6] A.E.M. Alaoui, A. Neme: Slamming load during vertical water entry at constant velocity. Proceedings of the International Offshore and Polar Engineering Conference, 2012.

[7] H. Luo, H. Wang, C.G. Soares: Numerical and experimental study of hydrodynamic impact and elastic response of one free-drop wedge with stiffened panels. Ocean Engineering 40, p. 1-14, 2012. https://doi.org/10.1016/j.oceaneng.2011.11.004.

[8] H. Luo, H. Wang, C.G. Soares: Comparative study of hydroelastic impact for one free-drop wedge with stiffened panels by experimental and explicit finite element methods. Proceedings of the International Conference on Offshore Mechanics and Arctic Engineering - OMAE, 2011. https://doi.org/10.1115/omae2011-49209.

[9] L.X. Mo, H. Wang, C.X. Jiang, C. Xu: Study on dropping test of wedge grillages with various types of stiffeness. Journal of Ship Mechanics 4, p. 394-40, 2011.

[10] H. Mutsuda, Y. Doi: Numerical simulation of dynamic response of structure caused by wave impact pressure using an Eulerian scheme with Lagrangian particles. Proceedings of the International Conference on Offshore Mechanics and Arctic Engineering - OMAE, 2009. https://doi.org/10.1115/omae2009-79736.

[11] Q. Yang, W. Qiu: Numerical Solution of 3-D Water Entry Problems with a Constrained Interpolation Profile Method. Journal of Offshore Mechanics and Arctic Engineering 134 (4), p. 041101, 2012. https://doi.org/10.1115/1.4006152.

[12] G. Wu: Numerical simulation for water entry of a wedge at varying speed by a high order boundary element method", Journal of Marine Science and Application 11 (2), p. 143-149, 2012. https://doi.org/10.1007/s11804-012-1116-3.

[13] Y.H. Wang, Z.Y. Wei: Numerical analysis for water entry of wedges based on a complex variable boundary element method. Explosion and Shock Waves 32 (1), p. 55-60, 2012.

[14] H. Luo, H. Wang, C.G. Soares: Numerical prediction of slamming loads on a rigid wedge subjected to water entry using an explicit finite element method. Advances in Marine Structures - Proceedings of the 3rd International Conference on Marine Structures, 2011.

[15] J. Gao, Y. Wang, K. Chen: Numerical simulation of the water entry of a wedge based on the Complex Variable Boundary Element Method. Applied Mechanics and Materials 90-93, p. 2507-2510, 2011. https://doi.org/10.4028/www.scientific.net/AMM.90-93.2507.

[16] P. Ghadimi, A. Saadatkhah, A. Dashtimanesh: Analytical solution of wedge water entry by using Schwartz-Christoffel conformal mapping. International Journal of Modeling, Simulation, and Scientific Computing 2 (3), p. 337-354, 2011. https://doi.org/10.1142/S1793962311000487.

[17] H. Sun, J. Zou, J. Zhuang, Q. Wang: The computation of water entry problem of prismatic planning vessels. 3rd International Workshop on Intelligent Systems and Applications - Proceedings, 2011.

[18] L. Qian, D. Causon, C. Mingham: Comments on an improved free surface capturing method based on Cartesian cut cell mesh for water-entry and exit problems. Proceedings of the Royal Society A: Mathematical, Physical and Engineering Sciences, 2012. https://doi.org/10.1098/rspa.2011.0379.

[19] Y. Li, Y. Li, S. Hu: Numerical simulation of water entry of two-dimensional body. Journal of Huazhong University of Science and Technology (Natural Science Edition), 2011.

[20] G.X. Wu, G.D. Xu, W.Y. Duan: A summary of water entry problem of a wedge based on the fully nonlinear velocity potential theory. Journal of Hydrodynamics 22 (5), p. 859-864, 2010. https://doi.org/10.1016/S1001-6058(10)60042-X.

[21] G.D. Xu, W.Y. Duan, G.X. Wu: Numerical simulation of oblique water entry of an asymmetrical wedge. Ocean Engineering 35, pp 1597-1603, 2008. https://doi.org/10.1016/j.oceaneng.2008.08.002.

[22] K. Gong, B. Wang, H. Liu: Modelling water entry of a wedge by multiphase SPH method. Proceedings of the Coastal Engineering Conference, 2010.

[23] K. Gong, H. Liu, B.l. Wang, Water entry of a wedge based on SPH model with an improved boundary treatment. Journal of Hydrodynamics 21(6), p. 750-757, 2009. https://doi.org/10.1016/S1001-6058(08)60209-7.

[24] S. Shao: Incompressible SPH simulation of water entry of a free-falling object. International Journal for Numerical Methods in Fluids 59, p. 91–115, 2009. https://doi.org/10.1002/fld.1813.

[25] M. Viviani, S. Brizzolara, L. Savio: Evaluation of slamming loads on a wedge-shaped section at different heel angles adopting SPH and RANSE methods. Maritime Industry, Ocean Engineering and Coastal Resources - Proceedings of the 12th International Congress of the International Maritime Association of the Mediterranean, 2008.

[26] L. Yin, Q. Qian: Free water impacting analysis of a two-dimensional wedge. Journal of Dalian Maritime University 1, p. 96-100, 2010.

[27] Q. Yang, W. Qiu: Numerical simulation of water impact for 2D and 3D bodies. Ocean Engineering 43, p. 82-89, 2012. https://doi.org/10.1016/j.oceaneng.2012.01.008.

[28] Q. Yang, W. Qiu: Numerical solutions of 2D and 3D slamming problems. Transactions of the Royal Institution of Naval Architects Part A: International Journal of Maritime Engineering 153, p. A89–A97, 2011.

[29] Q. Yang, W. Qiu: Computation of slamming forces on wedges of small deadrise angles using a CIP method. Proceedings of the International Offshore and Polar Engineering Conference, 2008.

[30] J. Wang, O. Faltinsen: Numerical investigation for air cavity formation during the high speed water entry of wedges. Proceedings of the International Conference on Offshore Mechanics and Arctic Engineering - OMAE, 2010. https://doi.org/10.1115/omae2010-20237.

[31] C.M. Rhie, W.L. Chow: Numerical study of the turbulent flow past an airfoil with trailing edge separation. AIAA Journal 21 (11), p. 1525-1532, 1983. https://doi.org/10.2514/3.8284.

[32] S.M. H. Karimian, G.E. Schneider: Pressure-based Computational Method for Compressible and Incompressible Flows. J. Thermo Physics and heat Transfer 8 (2), p. 267-274, 1994. https://doi.org/10.2514/3.533.

[33] T. Tveitnes, A.C. Fairlie-Clarke, K. Varyani: An experimental investigation into the constant velocity water entry of wedge-shaped sections. Ocean Engineering 35 (14-15), p. 1463–1478, 2008. https://doi.org/10.1016/j.oceaneng.2008.06.012.

Submitted: 23.03.2015. Roya Shademani, Parviz Ghadimi, pghadimi@aut.ac.ir

Accepted: 01.02.2016. Dept. Of Marine Technology, Amirkabir University of Technology, Tehran, Iran